Predictability of the Minimum Sea Ice Extent from winter Fram Strait Ice Area Export: Model vs Observations

Sandrine Trotechaud,[a] Bruno Tremblay[a,b] , James Williams[c] , Joy Romanski [c] , Anastasia Romanou[c] , Mitchell Bushuk[d] , William Merryfield[e] , Rym Msadek[f]

[a] *Department of Atmospheric and Oceanic Sciences, McGill University, Montréal, Québec, Canada*

[b] *Lamont-Doherty Earth Observatory, Columbia University, Palisades, New York*

[c] *NASA Goddard Institute for Space Studies, Columbia University, New York City, New York*

[d] *NOAA/Geophysical Fluid Dynamics Laboratory, Princeton, New Jersey*

[e] *Canadian Centre for Climate Modelling and Analysis, Environment and Climate Change Canada, Victoria, Canada*

[f] *Université de Toulouse, CNRS, CERFACS, Toulouse, France*

Corresponding author: Sandrine Trotechaud, sandrine.trotechaud@mail.mcgill.ca

ABSTRACT: We assess whether the observed seasonal predictability of September sea ice extent (SIE) arising from Fram Strait ice area export is present in Global Climate Models, namely the CESM2-LE, GISS-E2.1-G, GFDL FLOR-LE, CNRM-CM6-1, and CanESM5. Results show distinct periods where winter Fram Strait ice area export anomalies are negatively correlated with the May sea ice thickness anomalies along the Eurasian coastline, and the following September Arctic SIE, as in observations. Counter-intuitively, periods where winter Fram Strait ice area export anomalies are positively correlated with the following Sept SIE anomalies are also present in several models. This occurs early in the record when the mean Arctic sea ice thickness is large and ice area exported out of the Arctic (or recirculated in the Beaufort Gyre) survives the following summer melt leading to positive sea ice anomalies in the Greenland and Beaufort seas. Later in the record, when sea ice is thinner, winter Fram Strait ice area export anomalies are correlated with enhanced ridging and convergence of sea ice north of the Canadian Arctic Archipelago, leading to positive SIE anomalies in the late summer in the Lincoln Sea. Finally, there are several periods where the Fram Strait ice area export and coastal divergence are weakly coupled, resulting in no (statistically significant) seasonal predictability of the Sept SIE. In general, we find that the coupling between the Fram Strait ice area export and the Sept SIE is present across models and changes in the statistical relationship as a function of the mean Arctic sea ice thickness state.

1. Introduction

The Arctic has witnessed major changes in recent decades as a result of anthropogenic greenhouse gas emissions and subsequent polar amplification (Screen and Simmonds 2010; Dai et al. 2019). Since the beginning of the satellite era in the late '70s, the September sea ice extent (Sept SIE) has declined by -13% per decade (Fetterer 2017 updated daily), the area covered by multiyear ice (MYI) has decreased by more than 50% and the sea ice thickness has declined by 2m, with a loss of 1.2 m in the '80s and '90s alone (Kwok 2018). These changes have major implications for ocean-atmosphere heat and moisture fluxes, solar radiation absorbed at the surface, and the liquid freshwater storage in the Arctic, potentially affecting deep convection in the Greenland Sea and the global thermohaline circulation (Koenigk et al. 2005; Jahn and Holland 2013). Changes in the sea ice extent can also affect mid-latitude weather through atmospheric teleconnections (Coumou et al. 2018; Osborn 2010). Finally, the changing Arctic sea ice leading to new navigable passages affects tourism, economic and military operations (Stewart et al. 2009; Ebinger and Zambetakis 2009; Sharp 2011), as well as local ice-dependent and obligate species (Vincent et al. 2011).

The then record low September sea ice extent of 2007 marked the beginning of a new Arctic, with mainly ice-free conditions in the Chukchi and Beaufort Seas in summer, and increased interest for (sub-)seasonal forecasts of sea ice conditions (Stroeve et al. 2014). Coupled general circulation models with high-quality initialization can make skillful predictions when the Sept SIE is near the long-term linear trend but have difficulty making skillful predictions for anomalous years that fall outside of the linear trend such as in 2007 and 2012 (Stroeve et al. 2014). With the retreat of the sea ice cover, we see early signs of increased interannual variability, particularly in the Pacific sector of the Arctic (Desmarais and Tremblay 2021), making predictions of the Sept SIE more challenging. The inability of models to properly forecast September sea ice conditions for anomalous years (with respect to the linear trend) motivated the Study of Environmental Arctic Change (SEARCH) Sea Ice Outlook project with the objective of documenting and improving the skill of model forecasts using statistical, numerical and heuristic approaches.

The thinning of the sea ice has implications for sea ice thermodynamics (Massonnet et al. 2018) and dynamics (Spreen et al. 2011; Tremblay et al. 2015; Kwok and Cunningham 2012), which in

turn impact the skill of seasonal predictions. For instance, Williams et al. (2016) suggest that sea ice thickness at the onset of the melt season is a skillful predictor of the Sept SIE starting in the early '90s after the large export of MYI associated with record positive Arctic Oscillation (AO) indices (Rigor and Wallace 2004; Smedsrud et al. 2017; Spreen et al. 2011; Tremblay et al. 2015; Kwok and Cunningham 2012). Furthermore, Williams et al. (2016) relate May ice thickness anomalies to late winter coastal divergence along the Eurasian coastline that leads to new ice growth that does not have time to reach sufficient thickness to survive the following summer melt (see also Nikolaeva and Sesterikov 1970). This signal is then amplified by the ice-albedo feedback. Through that winter dynamic preconditioning, Williams et al. (2016) find at the pan-Arctic scale that both winter coastal divergence along the Eurasian coastline, and Fram Strait ice area export anomalies – a proxy for coastal divergence anomalies – are both well correlated with the following Sept SIE anomalies (respectively r = -0.58 and r = -0.72). This link between ice thickness at the onset of the melt season and seasonal predictability was supported by idealized model experiments, in which ice presence in different ice thickness categories led to predictability at different (sub-)seasonal time scales (Chevallier and Salas-Mélia 2012; Msadek et al. 2014; Dirkson et al. 2017; Bushuk and Giannakis 2017; Bonan et al. 2019). Recently, Kim et al. (2021) showed that late-winter coastal divergence leads to seasonal predictability in the Laptev Sea, in line with earlier results from Nikolaeva and Sesterikov (1970); Krumpen et al. (2013); Brunette et al. (2019), as well as the Beaufort and Kara Seas. The fact that the predictability from late winter coastal divergence is similar to that from June reflected shortwave radiation (Zhan and Davies 2017) supports the proposed link between late winter coastal divergence and the thickness anomalies at the onset of the melt season. In the Chukchi and eastern East Siberian Sea, subseasonal predictability of June and July sea ice area was shown to be associated with ocean heat transport anomalies through Bering Strait, with a resurgence of predictability in the fall when ventilation of sub-surface ocean heat takes place (Lenetsky et al. 2021).

In this study, we assess whether GCMs can reproduce the observed predictability of the Sept SIE from Fram Strait ice area export (FSIAE), a proxy for coastal divergence along the Eurasian coastline, in five global climate models: CESM2-LE, NASA GISS-E2.1-G, GFDL FLOR-LE, CNRM-CM6-1, and CanESM5. This link between ice export and ice formation in the ice

factory of the Arctic is an important coupled mode of variability between the atmosphere and the sea ice that is also at play on longer timescales; for instance in the transition to an ice-free Arctic. Failure to capture (or success in capturing) this coupling can highlight the weakness (or strength) in GCMs and guide future model development. We find periods with a significant negative correlation between the Fram Strait ice area export and Sept SIE anomalies in the five models studied as seen in observations, but also periods with a significant positive correlation for a thicker and thinner mean Arctic sea ice thickness state compared with the late 20th century.

The paper is structured as follows. The GCMs used in this study are described in section 2. The methods, results, and discussion are presented in section 3 and 4 respectively. The main conclusions are summarized in section 5.

2. Model Large Ensembles

a. CESM2 Large Ensemble (LENS2)

The Community Earth System Model Version 2 Large Ensemble (CESM2-LE) is a 100-member ensemble with a nominal spatial resolution of 1° covering the period 1850 to 2100. The atmospheric component of the model is the Community Atmosphere Model version 6 (CAM6) with a resolution of 1.25° in longitude, 0.9° in latitude, and 32 vertical levels. The Ocean and Ice components are the Parallel Ocean Program Version 2 (POP2) and the CICE Version 5.1.2 (CICE5) with a nominal 1° resolution. CICE5 uses the EVP rheology with an elliptical yield curve (ellipse aspect ratio e = 2, Hunke 2001), a normal flow rule and an ice thickness distribution with five categories (category limits of 0.0, 0.64, 1.39, 2.47 and 4.57 m, see Table 1). The grid is an Arakawa B-grid with a rotated pole located over Greenland to avoid the singularity over the North Pole (Fig. 1a). The model is run with CMIP6 historical forcing before 2014 and with CMIP6 SSP370 forcing scenarios after 2014 except for the aerosol forcing associated with biomass burning that was smoothed using an 11-year running mean filter in 50 of the 100 ensemble members during the 1990-2020 period. The smoothing of biomass burning has a distinct impact on the Arctic sea ice in the 1990-2020 interval with a slower decline of the September sea ice and cooler tropical Pacific (Rodgers et al. 2021; DeRepentigny et al. 2022). Following CESM1-LE, 20 ensemble members are initialized with micro-perturbations in atmospheric temperatures imposed for each

start year 1231, 1251, 1281, and 1301 of a pre-industrial simulation for a total of 80 ensemble members. The remaining 20 ensemble members are initialized using macro-perturbations, i.e., different initial conditions from independent restart files with a 10-year interval in start years ranging between 1001-1191 (Rodgers et al. 2021).

b. NASA GISS-E2.1-G

The NASA Goddard Institute for Space Studies ModelE Version 2.1-G (GISS-E2.1-G) is a 10-member ensemble with a nominal resolution of 2° in latitude and 2.5° in longitude covering the period 1850 to 2100. The atmospheric component of the model is the GISS-E2.1 and uses the non-interactive physics version 1 (NINT) with specified ozone and aerosol concentrations where the aerosol indirect effect is parameterized (Kelley et al. 2020; Miller et al. 2021). The ocean component of the model is the GISS Ocean V1 (GO1). The sea ice model uses the standard viscous plastic rheology with an elliptical yield curve (e = 2), a normal flow rule, a single ice-thickness category model (ice or open water), and a capping to prevent unrealistic ice build-up north of the Canadian Arctic Archipelago (CAA) (see Table 1) (Hibler 1979). The sea ice component uses the same grid as the atmosphere, i.e., an Arakawa B-grid on a standard spherical grid centered over the North and South Poles (Fig. 1b). The model is run with CMIP6 historical forcing before 2014 and CMIP6 SSP370 forcing scenarios after 2014. The ensemble members are initialized from a 451-year pre-industrial control run at 20-year intervals starting from the year 1 (Miller et al. 2021).

c. GFDL FLOR-LE

The Geophysical Fluid Dynamics Laboratory Forecast-oriented Low Ocean Resolution Large Ensemble (FLOR-LE) is a 30-member ensemble covering the period 1921-2100. The atmospheric component is the same as Coupled Model Version 2.5 (CM2.5) and has a nominal horizontal resolution of 0.5°. The ocean and sea ice components are the Modular Ocean Model Version 5 (MOM5) and the Sea Ice Simulator Version 1 (SIS1) from the Coupled Model Version 2.1 (CM2.1) with a nominal 1° spatial resolution. The sea ice model uses the EVP rheology with an elliptical yield curve (e = 2), a normal flow rule, and an ice thickness distribution with five categories (0.0,

0.1, 0.3, 0.7, and 1.1 m) but without redistribution between categories during ridging (See Table 1, Bushuk et al. 2021). The sea ice and ocean components use an Arakawa-B grid on a tri-polar grid with two poles located over Russia and the Canadian Arctic Archipelago (Fig. 1c). The model is run with CMIP5 historical forcing before 2005 and CMIP5 RCP8.5 radiative forcing scenarios after 2005. The ensemble members are initialized from a 1,160-year preindustrial control run at 10-year intervals from the simulation years 821–1,111 to ensure different phases of internal climate variability (Bushuk et al. 2020).

d. CNRM-CM6-1

The Centre National de Recherches Météorologiques Climate Model Version 6 (CNRM-CM6-1) jointly developed with the Centre Européen de Recherche et de Formation Avancée en Calcul Scientifique (CERFACS) is a 30-member ensemble with a nominal spatial resolution of 1° covering the period 1850 to 2100. Of the 30 ensemble members, 6 cover the full 1850 to 2100 time period and 24 ensemble members stop in 2039. The atmosphere component of the model is the ARPEGE-Climat Version 6.3 with a Gaussian grid and a nominal resolution of 1.4° at the Equator and 91 vertical levels. The ocean component of the model is the Nucleus for European Models of the Ocean (NEMO) Version 3.6 with a nominal 1° resolution. The sea ice component is Gelato 6 with the same horizontal grid as NEMO and uses the EVP model with an elliptical yield curve (e = 2), a normal flow rule and an ice thickness distribution with five categories (0.0, 0.3, 0.7, 1.2 and 2 m, Bouillon et al. 2009, See Table 1). The grid consists of an Arakawa-C grid on a tripolar grid (eOrca1 horizontal grid) with two quasi-isotropic bipolar grids south of 67° rather than the Mercator grid (Fig. 1d). The model is run with CMIP6 historical forcing before 2014 and CMIP6 SSP370 after 2014. The ensemble members are initialized from a 1000-year pre-industrial control simulation with different starting years in different phases of dominant modes of internal variability and with particular attention to the Atlantic multidecadal variability and the Pacific decadal variability (Voldoire et al. 2019).

e. CanESM5

The Canadian Earth System Model version 5 (CanESM5) developed by the Canadian Centre for Climate Modelling and Analysis (CCCma) is a 40-member ensemble covering the period 1850 to

Model	*P∗*	*Rheology*	*Ellipse Ratio*	*ITD category*	*Other*
CESM2-LE	27.5 kN/m^2	EVP	2	5 (0.0, 0.64, 1.39, 2.47 and 4.57 m)	-
GISS ModelE-G V2.1	27.5 kN/m^2	VP	2	1 (ice, no ice)	Capping of ice thickness to prevent building up along coastlines
GFDL FLOR-LE	27.5 kN/m^2	EVP	2	5 (0.0, 0.1, 0.3, 0.7 and 1.1 m)	No ridging parameterization and no prognostic melt ponds
CNRM-CM6-1	27.5 kN/m^2	EVP	2	5 (0.0, 0.30, 0.7, 1.2 and 2 m)	-
CanESM5	10 kN/m^2	EVP	2	1 (ice, no ice)	-

TABLE 1. Relevant sea ice parameters for the models studied

2100. Of the 40 ensemble members, 25 cover the full 1850 to 2100 time period and 15 ensemble members stop in 2014. The atmosphere component of the model is the Canadian Atmosphere Model Version 5 (CanAM5) with a spectral resolution of $\sim 2.8°$. The ocean component is a customized version of NEMO Version 3.4.1 (CanNEMO) where the ocean biochemistry is represented by the Canadian Model of Ocean Carbon (CMOC) and has a nominal resolution of $1°$ and the sea ice component is LIM2. LIM2 uses the EVP model with an elliptical yield curve (e = 2), a normal flow rule, and a single ice thickness category (ice or open water, see Table. 1). The grid consists of an Arakawa-C grid on a tripolar grid (eORCA1 horizontal grid, Fig. 1e). The model is run with CMIP6 historical forcing before 2014 and SSP370 forcing scenario after 2014. The ensemble members are initialized from a 2000-year pre-industrial control simulation with different starting years chosen at a 50-year interval (Swart et al. 2019).

3. Methods

a. Sea Ice Extent

The Arctic sea ice extent is defined as the total area of all grid cells with sea ice concentration (SIC) greater than 15% in the Northern Hemisphere.

b. Fram Strait Ice Area Export

The Fram Strait Ice Area Export (FSIAE) is used in this study as a proxy for coastal divergence along the Eurasian coastline as their anomalies are significantly correlated in observations (r =

0.79, Williams et al. 2016). The definition used in this study for the total winter sea ice area export through Fram Strait (FSIAE) is:

$$\text{FSIAE} = \sum_{k=1}^{N} V_{ice}(k) \cdot SIC(k) \cdot dL(k), \tag{1}$$

where N is the total number of grid cells across the Fram Strait, V_{ice} and dL are the meridional sea ice velocity and the length of the grid cell along the transect, SIC is the sea ice concentration and k is a running index (lat or lon) along the Strait (See Fig. 1). The FSIAE is computed for each winter month and summed from November to June. The location of the Fram Strait between models varies by at most 0.675° meridionally (~75 km). The results presented below are robust to the exact location of the Strait.

c. Mean Sea Ice Thickness

The May area-averaged sea ice thickness (see in Fig. 4b) is calculated from all grid cells north of 85° and with $SIC \geq 15\%$. The 85°N threshold is chosen as a representative Arctic mean excluding coastal regions.

d. Seasonal predictability and modes

We assess the seasonal predictability of the Sept SIE from the winter Fram Strait ice area export using a 20-year moving window correlation between anomalies with respect to their 5-year running mean (Fig. 5). Extending the window over which the anomalies are computed, or using the ensemble model mean as a reference for the anomalies, led to similar time series of the correlation, with only a slight vertical translation difference. The choice of 5 years for the window length used to compute the anomalies was made to study the interannual variability. We consider all periods that are correlated (statistically significant at the 95% level) for at least 10 years – with occasional excursions below the 95% significance level for a few years allowed, not more than approximately a third/fourth of the period's total length, to increase the sample size. All periods that are significantly correlated and with the same sign correlation are grouped together for each model and referred to in the following as positive and negative modes.

e. Difference maps

We use difference maps of the linearly detrended – over each identified period of significant correlation – May sea ice thickness composites between years with positive and negative anomalies in the linearly detrended FSIAE (1 σ away from the mean) in order to understand the link between the winter FSIAE and the following Sept SIE in transient simulations from different models with different mean climate. For each model, a composite is produced by taking the average over all the periods within a given mode (positive or negative, Fig. 7). The same procedure is repeated for the linearly detrended September SIC difference maps (Fig. 8).

4. Results and Discussion

a. Seasonality and projected change in SIE and SIT

All models simulate a SIE seasonal cycle, FSIAE, and sea ice thickness field that are in general agreement with observations (see Figs. 2-3). Notable biases in the mean state include a larger sea ice extent by 3-5 million km^2 in the GISS-E2.1-G model. A positive bias in winter FSIAE is found in all models, except CNRM-CM6-1. This is due, in part, to a too-broad Fram Strait (CESM2-LE) and faster meridional sea ice velocity (GISS-E2.1-G, FLOR-LE, and CanESM5, results not shown). Spatially, the sea ice thickness is in general agreement with the Pan-Arctic Ice Ocean Modeling and Assimilation System (PIOMAS) (Zhang and Rothrock 2003) with proper sea ice thickness gradient between the CAA and the Eurasian coastline and similar thickness levels, except for CNRM-CM6-1 that is considerably thinner (Fig. 3). It is worthy to mention that PIOMAS overestimates thin sea ice and underestimate thick sea ice(Schweiger et al. 2011), suggesting that all models show a generally too thin sea ice pack, except for CanESM5.

During the observational record, the Sept SIE is mostly within the envelope of internal variability for all models except the GISS-E2.1-G model (Fig. 4). CESM2-LE and CanESM5 reach a seasonally ice-free state – Sept SIE < 1 million km^2 for 5 consecutive years (as defined by the Intergovernmental Panel on Climate Change ice-free criteria) in the first half of the 21st century. The FLOR-LE and CNRM show a linear decline with a seasonally ice-free Arctic in the second half of the 21st century. The GISS-E2.1-G model does not reach a seasonally ice-free state before 2100, likely due to a positive bias in sea ice thickness and SIE in the 20th century. Of particular

Models		Mean length (years)	Frequency (%)	Total Frequency (%)
CESM2-LE	Negative	21.20	13.4	14.7
	Positive	15.74	1.3	
GISS-E2.1-G	Negative	30.51	16.1	22.7
	Positive	16.67	6.6	
FLOR-LE	Negative	29.87	39.6	39.6
CNRM-CM6-1	Negative	25.93	36.7	36.7
CanESM5	Negative	21.38	9.3	10.6
	Positive	16.67	1.3	

TABLE 2. Frequency of occurrence of periods with positive and negative correlation between winter FSIAE and Sept SIE anomalies.

interest is the absence of correlation between the projected decline in May SIT (and Sept SIE) and the mean 20th century May sea ice thickness. For instance, CanESM5 has the fastest decline in its May SIT (and Sept SIE) despite having the thickest (and the second most extensive sea ice cover) in its 20th century simulations.

b. Seasonal predictability of the Sept SIE from Winter FSIAE

From a total of 42,546 years of model simulations, the FSIAE is negatively – in line with recent decades (Williams et al. 2016) –, positively and not correlated with the Sept SIE for 7915, 549, and 34082 years, respectively. Counter-intuitively, we see periods of positive correlation between winter FSIAE and Sept SIE anomalies where larger winter FSIAE leads to larger Sept SIE the following September (discussion below, Fig. 5a-b-e). However, note that the corresponding frequency of occurrence – the amount of years correlated divided by the total amount of years of simulation – for negative correlations is 19% and positive correlations is 1%. The models' individual frequency of occurrence range from around 11%-15% for models with an early seasonally ice-free Arctic (CESM2-LE and CanESM5) to 37%-40% for models reaching a later ice-free Arctic (GFDL FLOR-LE, CNRM-CM6-1), suggesting a coupling between sea ice conditions and seasonal predictability skills of the winter FSIAE (see Table 2). Across all models, the negative mode occurs much more frequently than the positive mode and are generally longer (see Table 2).

The positive mode is observed when the sea ice cover is thickest (early 20th century) or thinnest (late 21st century), while the negative mode is mostly present for a mean sea ice thickness state that lies in between those extremes; one exception is the negative mode in the CanESM5 20th century simulations with a thick mean sea ice state (Fig. 6e). The positive and negative modes occur at different times depending on the model due to different mean sea ice thickness states. In thickness space (see Fig. 6), models mostly align, with positive modes present for ice thickness greater than 2.5 meters and thinner than 1.5 meters and negative modes for ice thickness ranging in between. Across all models, the negative mode occurs much more frequently than the positive mode.

1) Negative mode

Negative modes are present in all models and are associated with negative anomalies in the May sea ice thickness along the Eurasian coastline (the Arctic ice factory) when positive anomalies in the winter FSIAE are present (Fig. 7a-c-e-f-g). The negative anomalies in the May thickness in turn lead to negative anomalies in the September SIC in the same region, in line with the late winter coastal divergence mechanism proposed by Nikolaeva and Sesterikov (1970); Krumpen et al. (2013); Williams et al. (2016); Brunette et al. (2019) (Fig. 8a-c-e-f-g). Positive anomalies in winter FSIAE are also associated with positive anomalies in the May thickness north of the CAA due to ridging and convergence, and in the Greenland Sea due to larger export of thick sea ice through Fram Strait (Fig. 7a-c-e-f-g). For a mean climate with sea ice thickness in the medium range (1.5–2.5 m; see Fig. 6), the thickness anomalies in the Greenland Sea persist the following September, resulting in positive September SIC anomalies in this region. In terms of pan-Arctic SIE, these anomalies are relatively negligible compared to the reduced Sept SIE along the Eurasian coastline (Fig. 8a-c-e-f-g). Note that in the negative mode of the GISS-E2.1-G, ice appears to be restricted as it moves towards the Fram Strait (see positive/negative anomalies in SIC north/south of the strait, Fig. 8c). This pattern is consistent with the positive anomaly in sea ice thickness in the GISS model, which somewhat reduces the coupling between FSIAE and coastal divergence in the ice factory of the Arctic.

2) Positive mode

The positive modes occur either early in the record in models that have a positive bias in sea ice thickness (GISS-E2.1-G and the CanESM5) or late in the record in models with an early

transition to a seasonally ice-free Arctic (CESM2-LE and CanESM5, Fig. 4 and 6). There is no documented positive correlation between FSIAE, or coastal divergence, with the following Sept SIE in observations. Early in the modern observational record (80's and 90's), anomalous sea ice conditions in the Greenland and Beaufort seas and have been reported to be negatively correlated with sea ice extent in the Baffin Bay; an east-west seesaw associated with the North Atlantic Oscillation (Wang et al. 1994; Mysak et al. 1996; Deser et al. 2000). In the same period, a large tongue of sea ice extending northeastward in the Greenland Sea (the so-called Odden) was associated with the negative phase of the NAO and larger export of freshwater through the Fram Strait (e.g., late seventies Great Salinity Anomaly, see Rogers and Hung 2008), highlighting a link between the sea ice state and large-scale atmospheric circulation before the current transition to a seasonally ice-free Arctic.

Early in the record positive anomalies in winter FSIAE in CanESM5 and GISS-E2.1-G leads to positive anomalies in the May sea ice thickness in the Beaufort, Chukchi, and Lincoln seas (Fig. 7d,h). In the GISS-E2.1-G model, large winter FSIAE are associated with more recirculation of thick ice in the Beaufort Gyre and also more coastal divergence along the Eurasian coastline (Fig. 7d). This recirculation of thicker sea ice in the Beaufort Sea leads to positive SIE anomalies the following summer (Fig. 8d). Larger winter FSIAE also leads to larger export of sea ice through the Fram Strait into the Greenland Sea (Fig. 7d) and positive anomalies in the September sea ice concentration in the Greenland and Barents seas (Fig. 8d). Note that the May sea ice thickness anomalies along the Eurasian coastline result in near-zero anomalies in the September SIC in the GISS model because the mean thickness is larger than a typical summer melt rendering the winter FSIAE – Sept SIE coupling ineffective. By contrast, the negative mode predominates later in the simulation when the sea ice cover is thinner and the northern North Atlantic warms, ice exported through Fram Strait melts in the Greenland Sea and the reduced sea ice extent along the Eurasian coastline dominates (Fig. 8c). In a similar manner, positive anomalies in the winter FSIAE in CanESM5 are associated with positive anomalies in the May sea ice thickness in the Greenland and the Barents Seas and an increased September SIC in the same regions (Fig. 7h-8h). Again, the SIC anomaly signal in the same regions dominates the negative anomaly signal along the Eurasian

coastline.

Later in the record, when the Arctic approaches a seasonal ice-free cover, periods of positive mode are present both in the CESM2-LE and the CanESM5 models, the two first models that reach a seasonal ice-free cover in the first half of the 21st century (Fig. 4a). In the CESM2-LE, large winter FSIAE is associated with ridging north of the Canadian Arctic Archipelago leading to thicker sea ice that is more likely to survive the following summer (Fig. 6a and 8b). In a similar manner, periods are present in CanESM5 positive modes where positive anomalies in the winter FSIAE in CanESM5 lead to positive anomalies in the May sea ice thickness particularly north of Greenland, and a more extensive September SIC anomaly (Fig. 7i-8i). This is akin to the observed convergence of sea ice (also present in the PIOMAS reanalysis) in recent years as the sea ice thins, particularly north of the CAA and Greenland (Bitz et al. 2001; Kwok and Cunningham 2012; Zhang et al. 2012). This increased propensity for convergence is due to a thinner ice pack that is more likely to ridge and deform (Thorndike et al. 1975).

c. Discussion

The behavior of the models is in general agreement with the observations considering the length of the observational record and in the measure where we find several periods of negative correlation occurring in all models (see Table 2, Williams et al. 2016). However, the observed coefficient correlation (r=-0.72 Williams et al. 2016) is at the edge of what the models simulate (see Fig. 9), suggesting either that the observed coupling between winter FSIAE with the following Sept SIE is unusual in observation, or that the models are bias in a way to reduce this coupling. In addition, the frequency of occurrence of the significantly correlated periods is dependant on the models' sea ice conditions (see Table 2) and also explained by the print of internal variability of the models on the correlation coefficient (see Fig. 9).

Other than the negative periods identified in the models, the results show a broader range of behavior with FSIAE that can also be positively correlated with the Sept SIE both early and late in the record when a thick and thin sea ice cover is present. Specifically, models with thicker 20th century sea ice cover (CanESM5 and GISS-E2.1-G) show occasional periods of positive

correlation between FSIAE and SIE. These positive correlations arise due to the persistence of positive ice thickness anomalies in the Greenland Sea and Baffin Bay through the melting season, leading to positive anomalies in late summer SIC in these regions. The models with an early transition to a seasonally ice-free cover (CESM2-LE and CanESM5) show a positive correlation between FSIAE and SIE, which is explained by increased ridging and convergence of sea ice north of the CAA and Greenland which creates localized thickness anomalies in these regions that can survive the summer melt season. Our findings show re-emergence or memory of the system to anomalies in sea ice thickness that re-appears later as sea ice area anomalies, in the present case from the late winter to the late summer, as opposed to from fall to later winter (or from summer to summer) (Blanchard-Wrigglesworth et al. 2011a; Bushuk et al. 2017).

Past studies have shown the non-stationary aspect of the relationship between coastal divergence and the following Sept SIE, and similarly between the AO and the FSIAE (Williams et al. 2016; Smedsrud et al. 2017; Rigor and Wallace 2004; Jung and Hilmer 2001). Similarly here, we find that the relationship between the winter FSIAE with the following Sept SIE, i.e., the seasonal predictability skill of the winter FSIAE, is non-stationary, and depends on the sea ice regime, influencing both the sign of the correlation and frequency of occurrence of the positive and negative modes within each model (Fig. 6-9). An increase in frequency in the number of periods (and their length) within the positive to the negative modes (see Fig. 6) indicates an increased coupling between FSIAE and Sept SIE as the sea ice thins to moderate sea ice thickness within all models (except for CanESM5) supporting the hypothesis that a thinner sea ice cover is more mobile and hence more responsive to changes in atmospheric forcing (Fig. 6-9) (Rigor and Wallace 2004).

When the sea ice thins further, models show a loss in predictability during the transition to a seasonal ice cover (Fig. 9), in agreement with past studies that find a decrease in seasonal predictability as the sea ice thins due to increased variability in the sea ice extent in a warming climate (Goosse et al. 2009; Blanchard-Wrigglesworth et al. 2011b; Holland et al. 2011; Tietsche et al. 2013; Cheng et al. 2016). A recent study shows that the seasonal predictability is the outcome of two competing factors in CESM-LE, one that leads to increased skill as the sea ice

retreats from coastal regions where variability is large, and another that leads to decreased skill as small errors in thickness leads to large errors in sea ice area melt and hence, on SIE forecast skill (Holland et al. 2019). These two competing factors result in a sweet spot in the early 21st century, with optimal seasonal predictability skill (Holland et al. 2019). Similarly, we find a peak in the seasonal predictability in the thickness domain for each of the models at 2 meters in thickness for all models except CanESM5 (Fig. 6-9b-d-f-h-i).

Furthermore, in contrast with past studies reporting non-stationarity in the relationship between FSIAE and the AO or NAO (Smedsrud et al. 2017), we find a link between FSIAE anomalies and SLP patterns for all sea ice regimes within the significantly correlated periods. Indeed, results show that the winter SLP pattern associated with anomalously low linearly detrended FSIAE has a broad Beaufort Gyre, and years of anomalously high linearly detrended FSIAE have a broader Transpolar drift and a smaller and confined Beaufort Gyre in the western Arctic due to a deeper Icelandic low in the Arctic Ocean (Fig. 10-11). These two patterns are typical of a negative and positive AO mode respectively, highlighting the relationship between AO and winter FSIAE in the GCMs found in observations (Rigor et al. 2002; Kwok 2004; Williams et al. 2016; DeRepentigny et al. 2016). Regardless of the sign of the correlation within the significantly correlated periods, the coupling between the AO with the winter FSIAE lead to similar outcomes of the winter FSIAE on the following May sea ice thickness (see Fig. 7), suggesting similar winter preconditioning of the sea ice throughout the modes of significant correlation, again highlighting rather the impact of the sea ice thickness regime on the summer melt, and hence on the sign of the correlation.

Finally, the two models (GFDL FLOR-LE and CNRM-CM6-1) with the largest number of significantly correlated periods (with a frequency of occurrence respectively of 39.6% and 36.7%, see Table 2) are models that are closest to observations (thickness and extent) during the observational record and that reach a seasonal cover in the second half of the century only (Fig 4). In contrast, we have that CESM2-LE and CanESM5 have the lowest frequency with 14.7% and 10.6% respectively presumably due to an early transition to a seasonal ice cover in the first half of the 21st century, as well as a positive bias in sea ice for CanESM5 early in the record. We argue that the temporal changes in positive and negative modes distribution are due to thick or thin sea ice regime (see

Fig. 6) and that the two models with greater frequency (CNRM-CM6-1 and FLOR-LE) are the two models with mid-range thicknesses, corresponding to the peak in predictability (Fig. 6), reported by (Holland et al. 2019).

5. Conclusion

Late winter coastal divergence along the Eurasian coastline (referred to as the ice factory of the Arctic) – or the Fram Strait ice export, a proxy for coastal divergence in the ice factory – is a skillful predictor of the Sept SIE in observations (Williams et al. 2016). In this work, we use a 20-year moving window correlation between the FSIAE and the following Sept SIE anomalies to assess whether the observed seasonal predictability is also present in GCMs. To this end, we analyze output diagnostics from 5 GCM large ensembles. Results show that all models studied have some seasonal predictability skill of the Sept SIE from winter FSIAE with larger ice export resulting in lower May SIT along the Eurasian coastline, and hence lower Sept SIE as per observations (Nikolaeva and Sesterikov 1970; Krumpen et al. 2013; Williams et al. 2016; Brunette et al. 2019; Kim et al. 2021). Looking at GCMs over longer time scales and many ensemble members highlights new behaviors in the coupling between FSIAE and Sept SIE, namely occasional periods when larger FSIAE leads to larger Sept SIE. This coupling varies in time and appears as periods of positive, negative, or absence of significant correlations. Within the 5 large ensembles, we find 7915, 549, and 34082 years with negative, positive, and non-correlated modes between FSIAE and Sept SIE (see Table 2). Interestingly, the sign of the correlation changes through time depending on the sea ice thickness regime in contrast with observations presumably due to limitations in the length of the observational record and hence, of the sea ice thickness regime. Although, it is important to mention that the correlation coefficient can vary substantially between ensemble members with similar sea ice thickness regime due to the importance of internal variability (Fig. 9).

Results show that for mid-range ice thickness, as in recent decades, a statistically significant negative correlation between the winter FSIAE with the following Sept SIE is linked with coastal divergence and ice thickness anomalies along the Eurasian coastline as hypothesized in an earlier study by Nikolaeva and Sesterikov (1970). On the other end, when sea ice is thicker, positive and significant correlations are occasionally found and associated with the persistence of the sea ice

in the Greenland Sea or western Beaufort Gyre during the melt season when FSIAE is large and more ice recirculates in the Beaufort Gyre. Near a seasonal ice-free cover, the positive correlation between winter FSIAE and Sept SIE is associated with ridging north of CAA and in the Lincoln Sea which leads to thicker sea ice that survives the melt season in CESM2-LE and CanESM5. Finally, the GISS-E2.1-G suggests a restriction of sea ice by the Fram Strait in its negative mode due to a thick sea ice bias in its mean climate (Fig. 8c and 4a). While the large-scale atmospheric forcing and the winter preconditioning of the sea ice pack associated with the positive and negative mode are nearly identical (Fig. 7), it is rather the response of the sea ice to that atmospheric pattern that changes with time with different sea ice thickness regimes, i.e., thicker sea ice being less mobile and responsive to atmospheric forcing, while thinner sea ice is more responsive. These findings suggest that FSIAE will likely remain an important source of Sept SIE predictability over the coming decades.

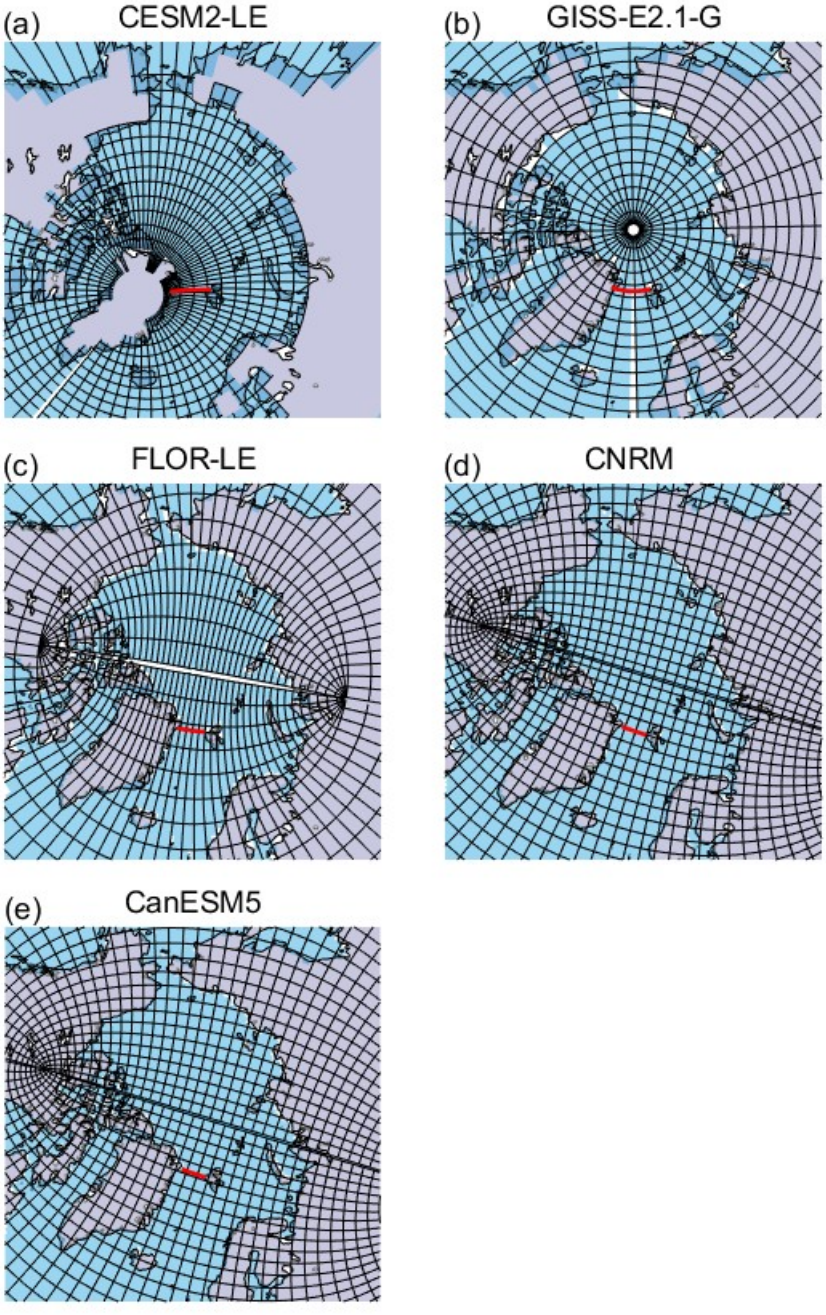

457 FIG. 1. Model domain, grid, and Fram Strait location (red) for (a) CESM2-LE, (b) GISS-E2.1-G, (c) FLOR-LE,
458 (d) CNRM-CM6-1 and (e) CanESM5. Model grid lines are shown for every four lines of latitude and longitude,
459 except for GISS-E2.1-G where each line of latitude is shown. The ocean mask is shown as blue shading.

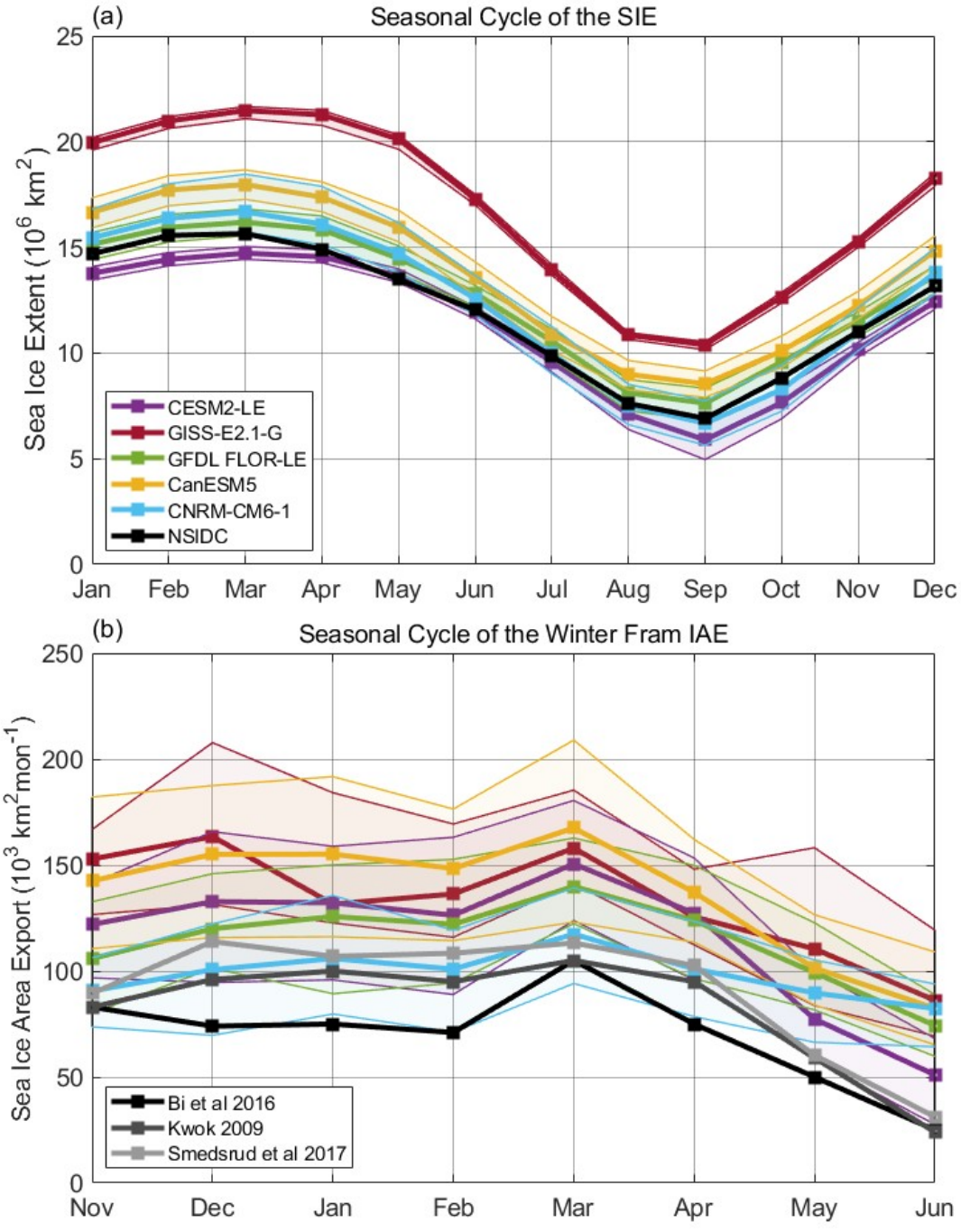

460 FIG. 2. (a) Ensemble Mean (thick lines) and range (shading) of the Sea Ice Extent seasonal cycle averaged over
461 1980-2000 for GISS-E2.1-G (red), CESM2-LE (purple), GFDL FLOR-LE (green), CanESM5 (yellow), CNRM-
462 CM6-1 (blue), and observations (black) from NSIDC averaged over 1980-2000 (b) Ensemble Mean Fram Strait
463 Ice Area Export seasonal cycle averaged over the 1980-2010 for GISS-E2.1-G (red), CESM2-LE (purple), GFDL
464 FLOR-LE (green), CanESM5 (yellow), CNRM-CM6-1 (blue), and estimates derived from observations (Bi et
465 al., 2016, 2004-2010, black; Kwok, 2009, 1979-2000, dark grey; Smedsrud et al., 2017, 1935-2014, light grey).

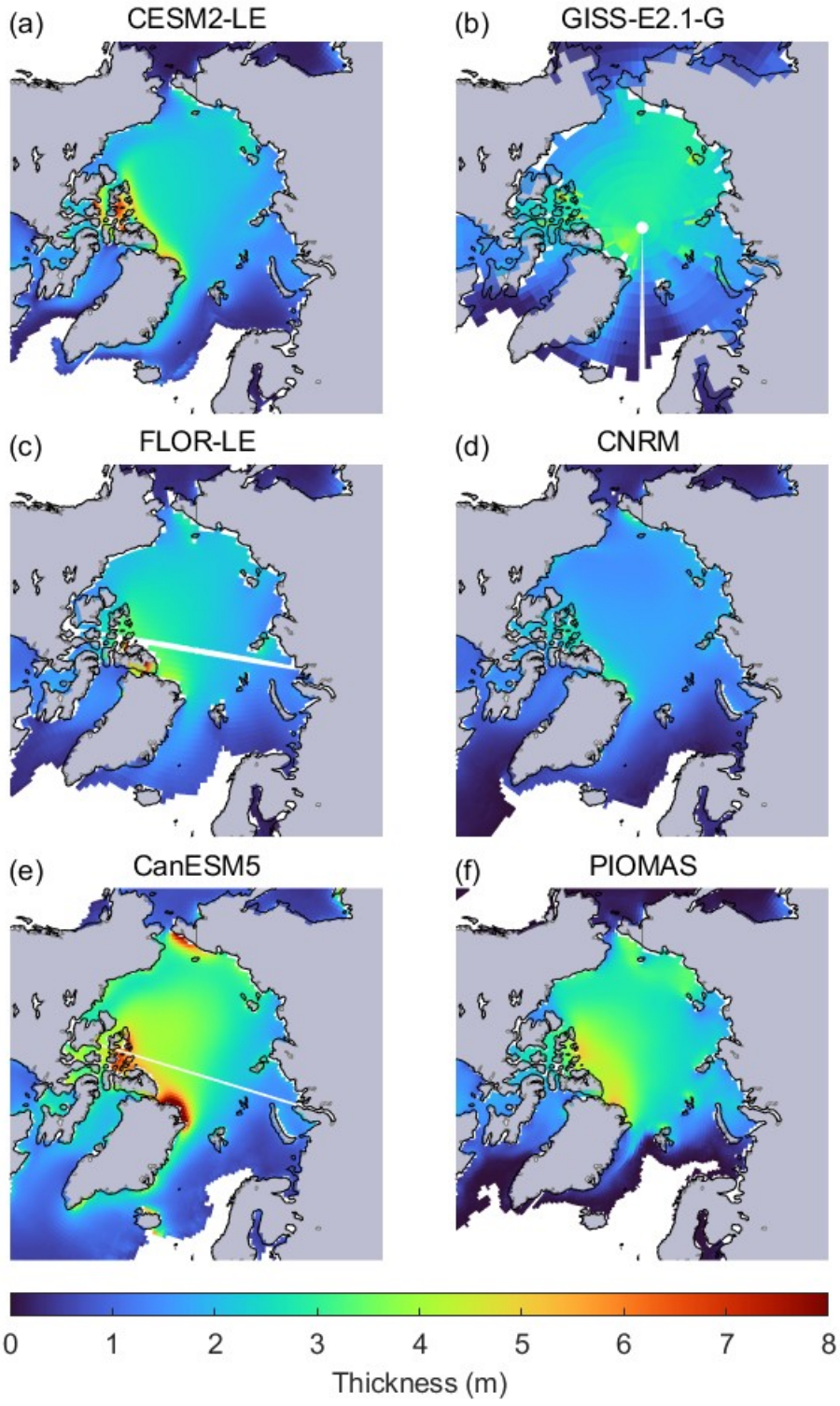

466 FIG. 3. Ensemble Mean spatial May Sea Ice Thickness within the sea ice pack (SIC>15%) averaged over 1980-
467 2000 for (a) CESM2-LE, (b) GISS-E2.1-G, (c) FLOR-LE, (d) CNRM-CM6-1, (e) CanESM5 and (f) PIOMAS
468 (Zhang and Rothrock 2003).

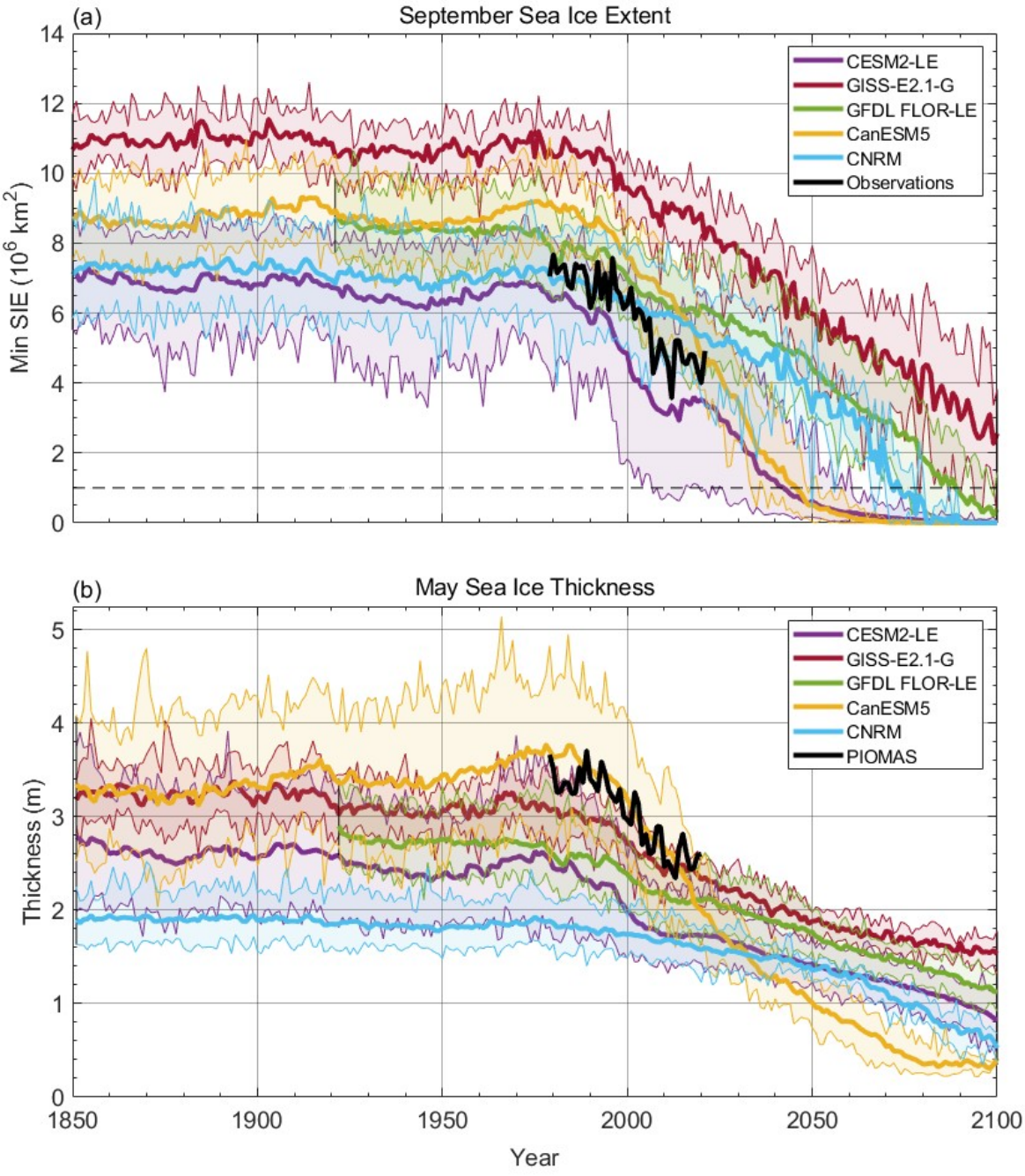

469 FIG. 4. (a) Ensemble Mean (thick lines) and range (shading) of the Sept SIE for CESM2-LE (purple), GISS-
470 E2.1-G (red), GFDL FLOR-LE (green), CanESM5 (yellow), CNRM-CM6-1 (blue) and observed Sept SIE from
471 passive microwave (NSIDC & NASA, black). The dashed grey line indicates an ice-free Arctic (1 million km^2)
472 as defined by the Intergovernmental Panel on Climate Change ice-free criteria. (b) Ensemble Mean May Sea
473 Ice Thickness north of 85N (SIC>15%) for CESM2-LE (purple), GISS-E2.1-G (red), GFDL FLOR-LE (green),
474 CanESM5 (yellow), CNRM-CM6-1 (blue) and PIOMAS (black).

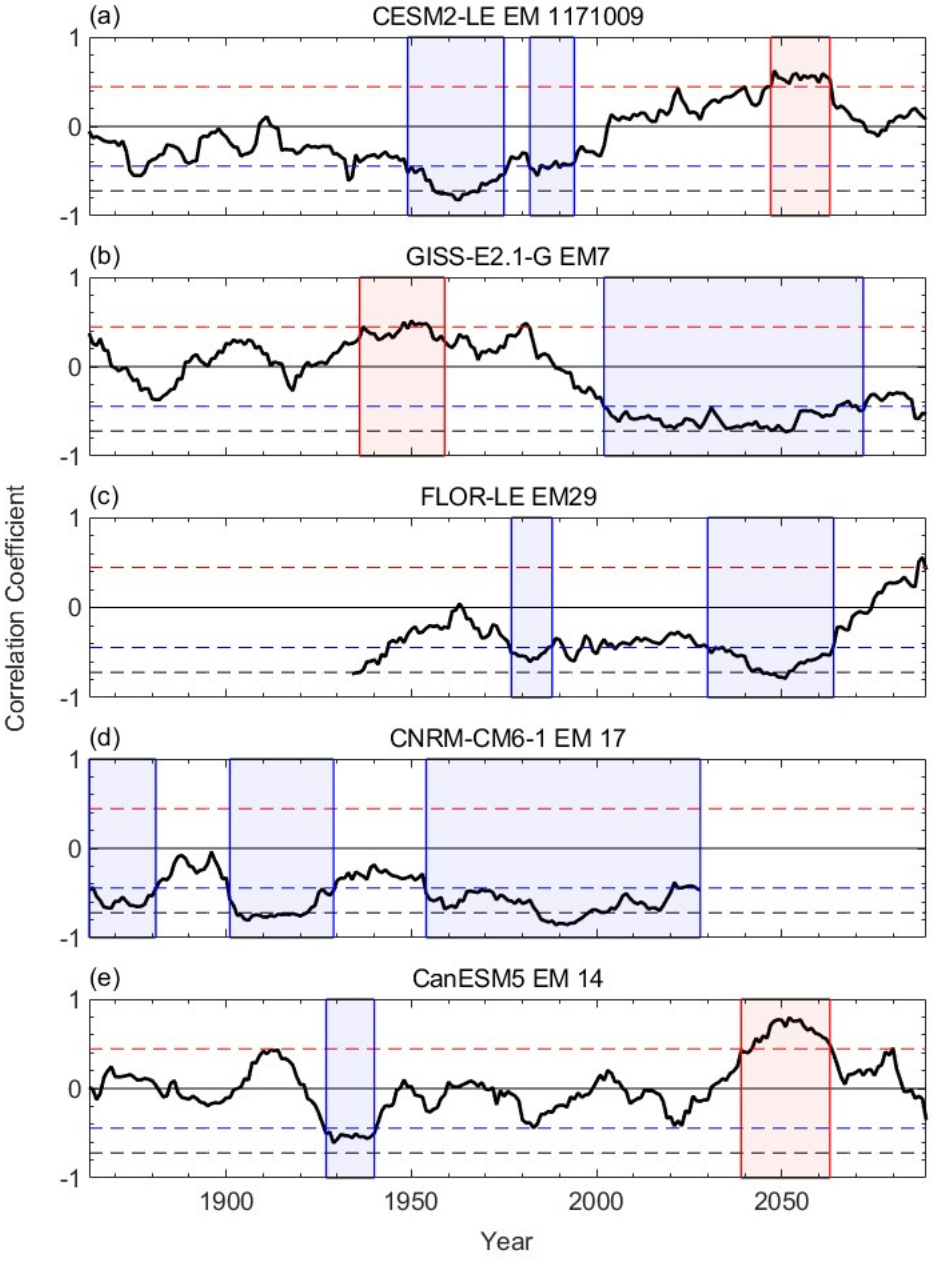

475 FIG. 5. 20-year sliding window correlation between the Nov-Jun Fram Strait Ice Area Export and the following
476 September Sea Ice Extent anomalies typical for one ensemble member of the (a) CESM2-LE EM 1171.009, (b)
477 GISS-E2.1-G EM7, (c) FLOR-LE EM29, (d) CNRM-CM6-1 EM17 and (e) CanESM5 EM14. The dashed lines
478 (blue and red) represent 95% significance level (p-value = 0.05). The black dashed line represents the correlation
479 coefficient between the FSIAE and the following Sept. SIE anomalies found in Williams et al. (2016). Shaded
480 areas indicate periods of at least 10 years that are negatively (blue) and positively (red) correlated ($p<0.05$)
481 excursions outside of the threshold for a few years allowed. In the following, we refer to the grouping of periods
482 between sea ice area export and Sept SIE that are positively (negatively) correlated as positive (negative) mode.

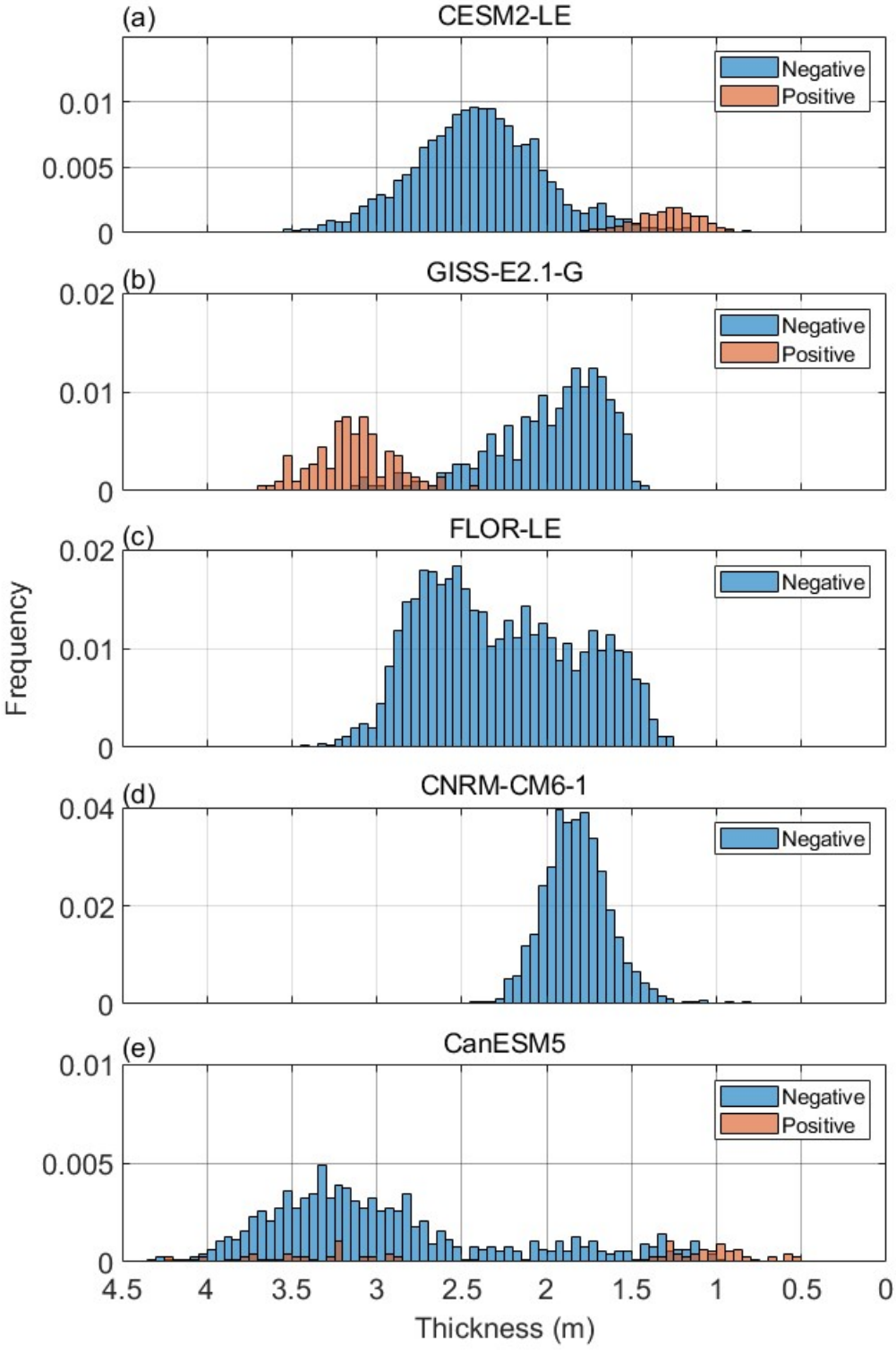

483 FIG. 6. Normalized distribution (by the total number of years per model) of the positive (orange) and negative
484 mode (blue) as a function of the May mean thickness north of 85°N time period in (a) CESM2-LE, (b) GISS-
485 E2.1-G, (c) FLOR-LE, (d) CNRM-CM6-1 and (e) CanESM5.

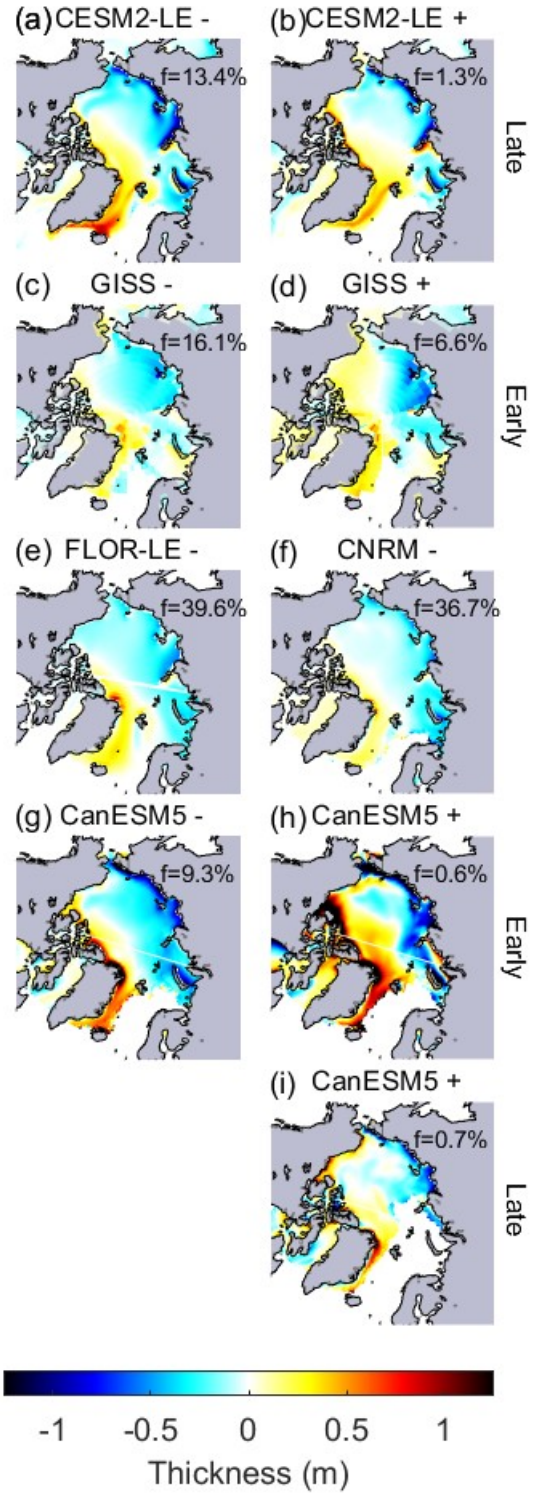

FIG. 7. Detrended May sea ice thickness difference between extreme years (|FSIAE|> σ) of the mean Nov-Jun FSIAE averaged over all the periods with positive modes in the early 20th century (d,h), the mid 21st century (b,i) and negative modes for (a) CESM2-LE, (c) the GISS-E2.1-G, (e) FLOR-LE, (f) CNRM and (g) CanESM5. The frequency of occurrence of the mode is shown in the top-right corner of each map (see Table 2).

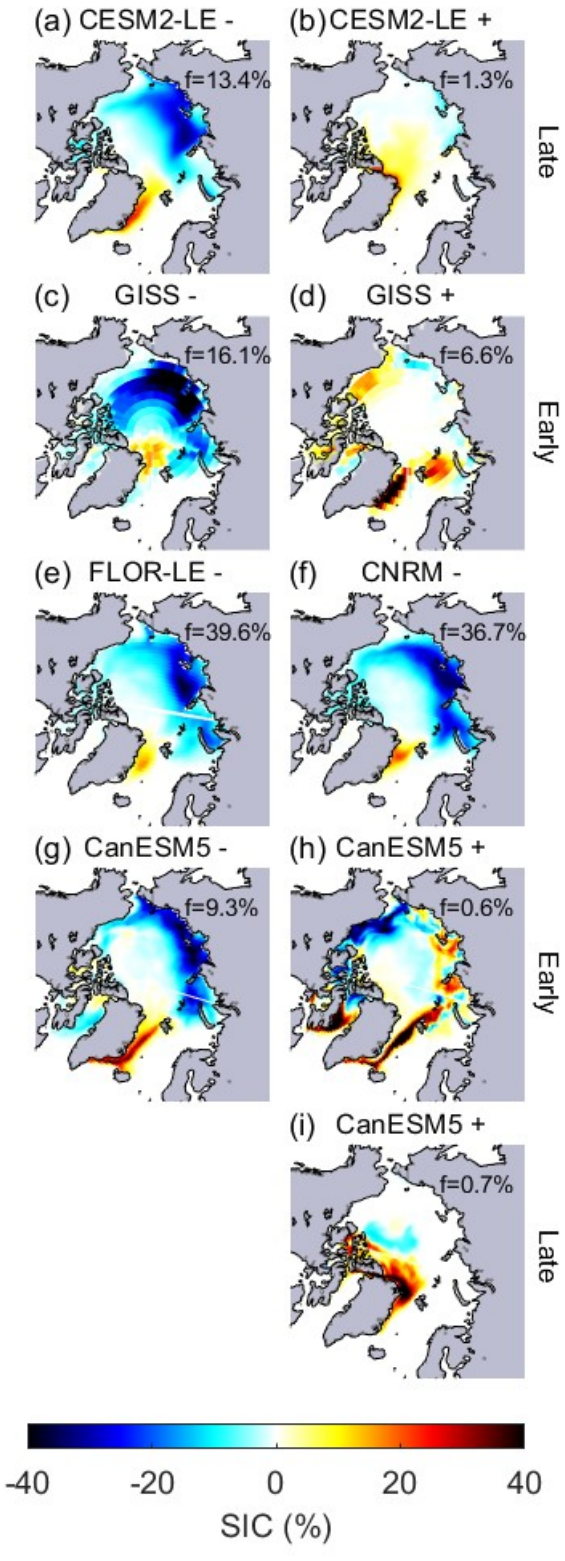

FIG. 8. Detrended September sea ice concentration difference between extreme years (|FSIAE|> σ) of the mean Nov-Jun FSIAE averaged over all the periods with positive modes early 20th century (d,h), mid 21st century (b,i) and negative modes for (a) CESM2-LE, (c) the GISS-E2-1-G, (e) FLOR-LE, (f) CNRM and (g) CanESM5. The frequency of occurrence of the mode is shown in the top-right corner of each map (see Table 2).

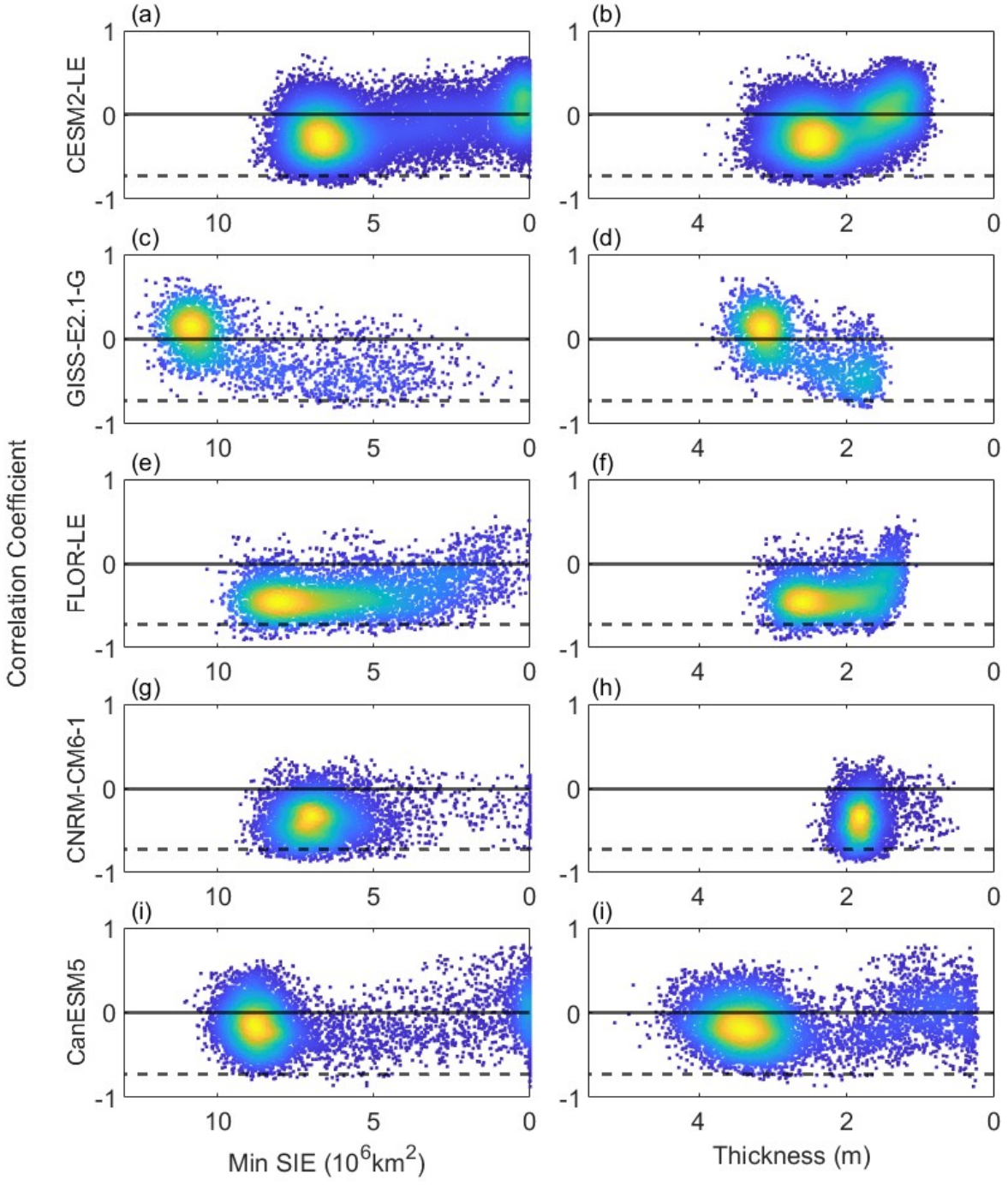

494 FIG. 9. Scatterplot of the correlation coefficient between the Nov-Jun FSIAE and Sept. SIE anomalies (see
495 Fig. 5) for all ensemble members as a function of the Sept SIE (first column) and the May mean thickness north
496 of 85°N (second column). The dashed line represents the correlation coefficient between the FSIAE and the
497 following Sept. SIE anomalies found in Williams et al. (2016)

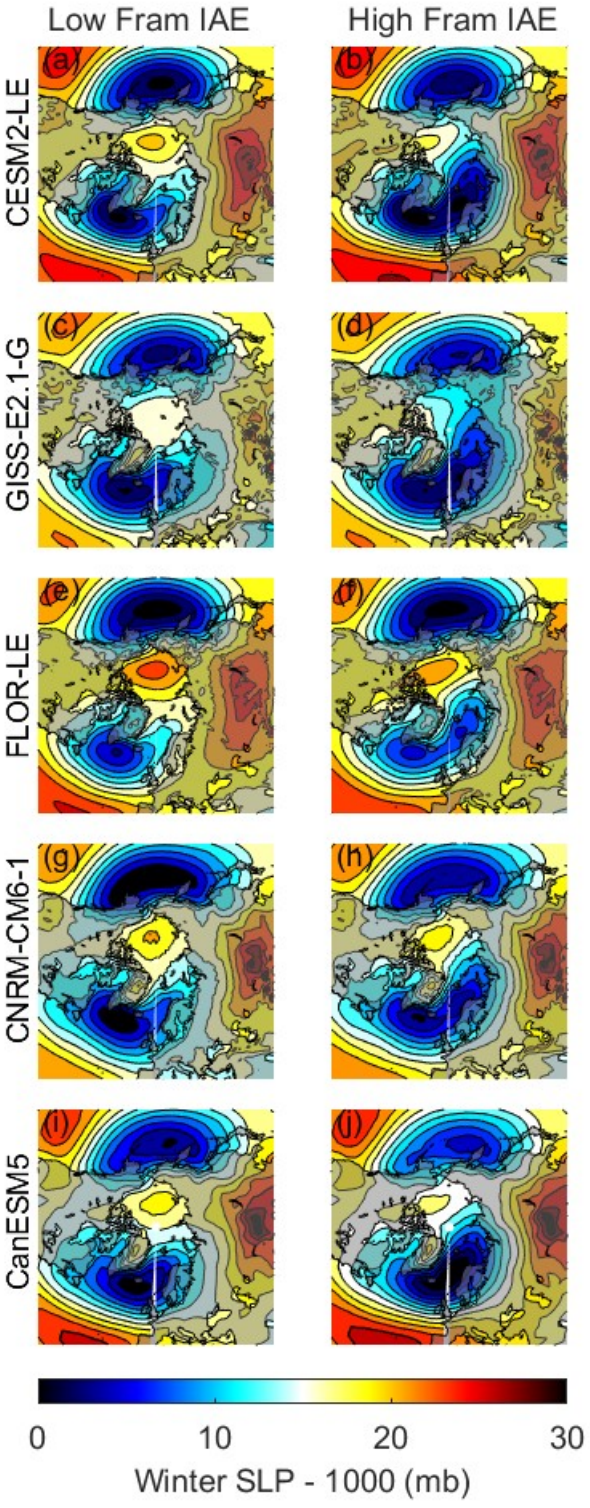

498 FIG. 10. Nov-Jun mean sea level pressure averaged over extreme years of the Nov-Jun FSIAE (|FSIAE|> σ)
499 averaged over all the periods within the negative modes for CESM2-LE (1st row), GISS-E2.1-G (2nd row),
500 FLOR-LE (3rd row), CNRM-CM6-1 (4th row) and CanESM5 (5th row).

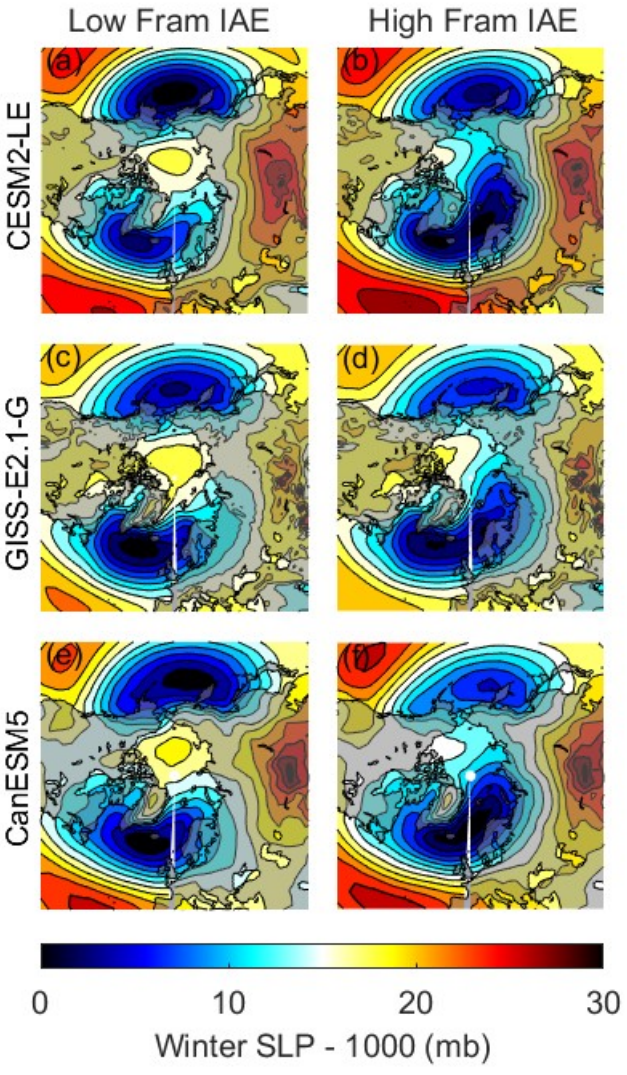

501 FIG. 11. Nov-Jun mean sea level pressure averaged over extreme years of the Nov-Jun FSIAE (|FSIAE|> σ)
502 averaged over all the periods within the positive modes for CESM2-LE (1st row), GISS-E2.1-G (2nd row) and
503 CanESM5 (3rd row).

Acknowledgments.

Data availability statement.

References

Bitz, C. M., M. M. Holland, A. J. Weaver, and M. Eby, 2001: Simulating the ice-thickness distribution in a coupled climate model. *Journal of Geophysical Research: Oceans*, **106 (C2)**, 2441–2463, https://doi.org/10.1029/1999jc000113, URL https://doi.org/10.1029/1999jc000113.

Blanchard-Wrigglesworth, E., K. C. Armour, C. M. Bitz, and E. DeWeaver, 2011a: Persistence and inherent predictability of arctic sea ice in a GCM ensemble and observations. *Journal of Climate*, **24 (1)**, 231–250, https://doi.org/10.1175/2010jcli3775.1, URL https://doi.org/10.1175/2010jcli3775.1.

Blanchard-Wrigglesworth, E., C. M. Bitz, and M. M. Holland, 2011b: Influence of initial conditions and climate forcing on predicting arctic sea ice. *Geophysical Research Letters*, **38 (18)**, n/a–n/a, https://doi.org/10.1029/2011gl048807, URL https://doi.org/10.1029/2011gl048807.

Bonan, D. B., M. Bushuk, and M. Winton, 2019: A spring barrier for regional predictions of summer arctic sea ice. *Geophysical Research Letters*, **46 (11)**, 5937–5947, https://doi.org/10.1029/2019gl082947, URL https://doi.org/10.1029/2019gl082947.

Bouillon, S., M. Á. M. Maqueda, V. Legat, and T. Fichefet, 2009: An elastic–viscous–plastic sea ice model formulated on arakawa b and c grids. *Ocean Modelling*, **27 (3-4)**, 174–184, https://doi.org/10.1016/j.ocemod.2009.01.004, URL https://doi.org/10.1016/j.ocemod.2009.01.004.

Brunette, C., B. Tremblay, and R. Newton, 2019: Winter coastal divergence as a predictor for the minimum sea ice extent in the laptev sea. *J. Climate*, **32**, https://doi.org/10.1175/JCLI-D-18-0169.1.

Bushuk, M., and D. Giannakis, 2017: The seasonality and interannual variability of arctic sea ice reemergence. *Journal of Climate*, **30 (12)**, 4657–4676, https://doi.org/10.1175/jcli-d-16-0549.1, URL https://doi.org/10.1175/jcli-d-16-0549.1.

Bushuk, M., R. Msadek, M. Winton, G. A. Vecchi, R. Gudgel, A. Rosati, and X. Yang, 2017: Skillful regional prediction of arctic sea ice on seasonal timescales. *Geophysical Research*

Letters, **44 (10)**, 4953–4964, https://doi.org/10.1002/2017gl073155, URL https://doi.org/10.1002/2017gl073155.

Bushuk, M., M. Winton, D. B. Bonan, E. Blanchard-Wrigglesworth, and T. L. Delworth, 2020: A mechanism for the arctic sea ice spring predictability barrier. *Geophysical Research Letters*, **47**, https://doi.org/10.1029/2020GL088335.

Bushuk, M., and Coauthors, 2021: Seasonal prediction and predictability of regional antarctic sea ice. *Journal of Climate*, 1–68, https://doi.org/10.1175/jcli-d-20-0965.1, URL https://doi.org/10.1175/jcli-d-20-0965.1.

Cheng, W., E. Blanchard-Wrigglesworth, C. M. Bitz, C. Ladd, and P. J. Stabeno, 2016: Diagnostic sea ice predictability in the pan-arctic and u.s. arctic regional seas. *Geophysical Research Letters*, **43 (22)**, https://doi.org/10.1002/2016gl070735, URL https://doi.org/10.1002/2016gl070735.

Chevallier, M., and D. Salas-Mélia, 2012: The role of sea ice thickness distribution in the arctic sea ice potential predictability: A diagnostic approach with a coupled GCM. *Journal of Climate*, **25 (8)**, 3025–3038, https://doi.org/10.1175/jcli-d-11-00209.1, URL https://doi.org/10.1175/jcli-d-11-00209.1.

Coumou, D., G. D. Capua, S. Vavrus, L. Wang, and S. Wang, 2018: The influence of arctic amplification on mid-latitude summer circulation. *Nature Communications*, **9 (1)**, https://doi.org/10.1038/s41467-018-05256-8, URL https://doi.org/10.1038/s41467-018-05256-8.

Dai, A., D. Luo, M. Song, and J. Liu, 2019: Arctic amplification is caused by sea-ice loss under increasing CO2. *Nature Communications*, **10 (1)**, https://doi.org/10.1038/s41467-018-07954-9, URL https://doi.org/10.1038/s41467-018-07954-9.

DeRepentigny, P., L. B. Tremblay, R. Newton, and S. Pfirman, 2016: Patterns of sea ice retreat in the transition to a seasonally ice-free arctic. *Journal of Climate*, **29 (19)**, 6993–7008, https://doi.org/10.1175/jcli-d-15-0733.1, URL https://doi.org/10.1175/jcli-d-15-0733.1.

DeRepentigny, P., and Coauthors, 2022: Enhanced simulated early 21st century arctic sea ice loss due to CMIP6 biomass burning emissions. *Science Advances*, **8 (30)**, https://doi.org/10.1126/sciadv.abo2405, URL https://doi.org/10.1126/sciadv.abo2405.

Deser, C., J. E. Walsh, and M. S. Timlin, 2000: Arctic sea ice variability in the context of recent atmospheric circulation trends. *Journal of Climate*, **13 (3)**, 617–633, https://doi.org/10.1175/1520-0442(2000)013<0617:asivit>2.0.co;2, URL https://doi.org/10.1175/1520-0442(2000)013<0617:asivit>2.0.co;2.

Desmarais, A., and B. Tremblay, 2021: Assessment of decadal variability in sea ice in the community earth system model against a long-term regional observational record: implications for the predictability of an ice-free arctic. *Journal of Climate*, https://doi.org/10.1175/jcli-d-20-0561.1, URL https://doi.org/10.1175/jcli-d-20-0561.1.

Dirkson, A., W. J. Merryfield, and A. Monahan, 2017: Impacts of sea ice thickness initialization on seasonal arctic sea ice predictions. *Journal of Climate*, **30 (3)**, 1001–1017, https://doi.org/10.1175/jcli-d-16-0437.1, URL https://doi.org/10.1175/jcli-d-16-0437.1.

Ebinger, C. K., and E. Zambetakis, 2009: The geopolitics of arctic melt. *International Affairs*, **85 (6)**, 1215–1232, https://doi.org/10.1111/j.1468-2346.2009.00858.x, URL https://doi.org/10.1111/j.1468-2346.2009.00858.x.

Fetterer, F. K. K. M. W. S. M. W. A., 2017 updated daily: Sea ice index, version 3. NSIDC, URL https://nsidc.org/data/G02135/versions/3, https://doi.org/10.7265/N5K072F8.

Goosse, H., O. Arzel, C. M. Bitz, A. de Montety, and M. Vancoppenolle, 2009: Increased variability of the arctic summer ice extent in a warmer climate. *Geophysical Research Letters*, **36 (23)**, https://doi.org/10.1029/2009gl040546, URL https://doi.org/10.1029/2009gl040546.

Hibler, W. D., 1979: A dynamic thermodynamic sea ice model. *Journal of Physical Oceanography*, **9 (4)**, 815–846, https://doi.org/10.1175/1520-0485(1979)009<0815:adtsim>2.0.co;2, URL https://doi.org/10.1175/1520-0485(1979)009<0815:adtsim>2.0.co;2.

Holland, M. M., D. A. Bailey, and S. Vavrus, 2011: Inherent sea ice predictability in the rapidly changing arctic environment of the community climate system model, version 3. *Climate Dynamics*, **36 (7-8)**, 1239–1253, https://doi.org/10.1007/s00382-010-0792-4, URL https://doi.org/10.1007/s00382-010-0792-4.

Holland, M. M., L. Landrum, D. Bailey, and S. Vavrus, 2019: Changing seasonal predictability of arctic summer sea ice area in a warming climate. *Journal of Climate*, **32 (16)**, 4963–4979, https://doi.org/10.1175/jcli-d-19-0034.1, URL https://doi.org/10.1175/jcli-d-19-0034.1.

Hunke, E. C., 2001: Viscous–plastic sea ice dynamics with the EVP model: Linearization issues. *Journal of Computational Physics*, **170 (1)**, 18–38, https://doi.org/10.1006/jcph.2001.6710, URL https://doi.org/10.1006/jcph.2001.6710.

Jahn, A., and M. M. Holland, 2013: Implications of arctic sea ice changes for north atlantic deep convection and the meridional overturning circulation in CCSM4-CMIP5 simulations. *Geophysical Research Letters*, **40 (6)**, 1206–1211, https://doi.org/10.1002/grl.50183, URL https://doi.org/10.1002/grl.50183.

Jung, T., and M. Hilmer, 2001: The link between the north atlantic oscillation and arctic sea ice export through fram strait. *Journal of Climate*, **14 (19)**, 3932–3943, https://doi.org/10.1175/1520-0442(2001)014<3932:tlbtna>2.0.co;2, URL https://doi.org/10.1175/1520-0442(2001)014<3932:tlbtna>2.0.co;2.

Kelley, M., G. A. Schmidt, L. S. Nazarenko, S. E. Bauer, R. Ruedy, and G. L. R. et al., 2020: Giss-e2.1: Configurations and climatology. *Journal of Advances in Modeling Earth Systems*, **12**, https://doi.org/https://doi.org/10.1029/2019MS002025.

Kim, R., B. Tremblay, C. Brunette, and R. Newton, 2021: A regional seasonal forecast model of arctic minimum sea ice extent: Reflected solar radiation vs. late winter coastal divergence. *Journal of Climate*, 1, https://doi.org/10.1175/jcli-d-20-0846.1, URL https://doi.org/10.1175/jcli-d-20-0846.1.

Koenigk, T., U. Mikolajewicz, H. Haak, and J. Jungclaus, 2005: Variability of fram strait sea ice export: causes, impacts and feedbacks in a coupled climate model. *Climate Dynamics*, **26 (1)**, 17–34, https://doi.org/10.1007/s00382-005-0060-1, URL https://doi.org/10.1007/s00382-005-0060-1.

Krumpen, T., M. Janout, K. I. Hodges, R. Gerdes, F. Girard-Ardhuin, J. A. Hölemann, and S. Willmes, 2013: Variability and trends in laptev sea ice outflow between 1992–2011. *The*

Cryosphere, **7 (1)**, 349–363, https://doi.org/10.5194/tc-7-349-2013, URL https://doi.org/10.5194/tc-7-349-2013.

Kwok, R., 2004: Fram strait sea ice outflow. *Journal of Geophysical Research*, **109 (C1)**, https://doi.org/10.1029/2003jc001785, URL https://doi.org/10.1029/2003jc001785.

Kwok, R., 2018: Arctic sea ice thickness, volume, and multiyear ice coverage: losses and coupled variability (1958–2018). *Environmental Research Letters*, **13 (10)**, 105 005, https://doi.org/10.1088/1748-9326/aae3ec, URL https://doi.org/10.1088/1748-9326/aae3ec.

Kwok, R., and G. Cunningham, 2012: Deformation of the arctic ocean ice cover after the 2007 record minimum in summer ice extent. *Cold Regions Science and Technology*, **76-77**, 17–23, https://doi.org/10.1016/j.coldregions.2011.04.003, URL https://doi.org/10.1016/j.coldregions.2011.04.003.

Lenetsky, J. E., B. Tremblay, C. Brunette, and G. Meneghello, 2021: Subseasonal predictability of arctic ocean sea ice conditions: Bering strait and ekman-driven ocean heat transport. *Journal of Climate*, **34 (11)**, 4449–4462, https://doi.org/10.1175/jcli-d-20-0544.1, URL https://doi.org/10.1175/jcli-d-20-0544.1.

Massonnet, F., M. Vancoppenolle, H. Goosse, D. Docquier, T. Fichefet, and E. Blanchard-Wrigglesworth, 2018: Arctic sea-ice change tied to its mean state through thermodynamic processes. *Nature Climate Change*, **8 (7)**, 599–603, https://doi.org/10.1038/s41558-018-0204-z, URL https://doi.org/10.1038/s41558-018-0204-z.

Miller, R. L., and Coauthors, 2021: CMIP6 historical simulations (1850–2014) with GISS-e2.1. *Journal of Advances in Modeling Earth Systems*, **13 (1)**, https://doi.org/10.1029/2019ms002034, URL https://doi.org/10.1029/2019ms002034.

Msadek, R., G. A. Vecchi, M. Winton, and R. G. Gudgel, 2014: Importance of initial conditions in seasonal predictions of arctic sea ice extent. *Geophysical Research Letters*, **41 (14)**, 5208–5215, https://doi.org/10.1002/2014gl060799, URL https://doi.org/10.1002/2014gl060799.

Mysak, L., R. Ingram, J. Wang, and A. van der Baaren, 1996: The anomalous sea-ice extent in hudson bay, baffin bay and the labrador sea during three simultaneous NAO and ENSO episodes.

Atmosphere-Ocean, **34 (2)**, 313–343, https://doi.org/10.1080/07055900.1996.9649567, URL https://doi.org/10.1080/07055900.1996.9649567.

Nikolaeva, A. J., and N. P. Sesterikov, 1970: A method of calculation of ice conditions (on the example of the laptev sea). *Ice Forecasting Techniques for the Arctic Seas*, 150–230.

Osborn, T. J., 2010: Winter 2009/2010 temperatures and a record-breaking north atlantic oscillation index. *Weather*, **66 (1)**, 19–21, https://doi.org/10.1002/wea.660, URL https://doi.org/10.1002/wea.660.

Rigor, I. G., and J. M. Wallace, 2004: Variations in the age of arctic sea-ice and summer sea-ice extent. *Geophysical Research Letters*, **31 (9)**, n/a–n/a, https://doi.org/10.1029/2004gl019492, URL https://doi.org/10.1029/2004gl019492.

Rigor, I. G., J. M. Wallace, and R. L. Colony, 2002: Response of sea ice to the arctic oscillation. *Journal of Climate*, **15 (18)**, 2648–2663, https://doi.org/10.1175/1520-0442(2002)015<2648:rositt>2.0.co;2, URL https://doi.org/10.1175/1520-0442(2002)015<2648:rositt>2.0.co;2.

Rodgers, K. B., and Coauthors, 2021: Ubiquity of human-induced changes in climate variability. *Earth Syst. Dynam.*, **12**, 1393–1411, https://doi.org/10.5194/esd-12-1393-2021.

Rogers, J. C., and M.-P. Hung, 2008: The odden ice feature of the greenland sea and its association with atmospheric pressure, wind, and surface flux variability from reanalyses. *Geophysical Research Letters*, **35 (8)**, https://doi.org/10.1029/2007gl032938, URL https://doi.org/10.1029/2007gl032938.

Schweiger, A., R. Lindsay, J. Zhang, M. Steele, H. Stern, and R. Kwok, 2011: Uncertainty in modeled arctic sea ice volume. *Journal of Geophysical Research*, **116**, https://doi.org/10.1029/2011jc007084, URL https://doi.org/10.1029/2011jc007084.

Screen, J. A., and I. Simmonds, 2010: The central role of diminishing sea ice in recent arctic temperature amplification. *Nature*, **464 (7293)**, 1334–1337, https://doi.org/10.1038/nature09051, URL https://doi.org/10.1038/nature09051.

Sharp, T. L., 2011: The implications of ice melt on arctic security. *Defence Studies*, **11 (2)**, 297–322, https://doi.org/10.1080/14702436.2011.590318, URL https://doi.org/10.1080/14702436.2011.590318.

Smedsrud, L. H., M. H. Halvorsen, J. C. Stroeve, R. Zhang, and K. Kloster, 2017: Fram strait sea ice export variability and september arctic sea ice extent over the last 80 years. *The Cryosphere*, **11 (1)**, 65–79, https://doi.org/10.5194/tc-11-65-2017, URL https://doi.org/10.5194/tc-11-65-2017.

Spreen, G., R. Kwok, and D. Menemenlis, 2011: Trends in arctic sea ice drift and role of wind forcing: 1992-2009. *Geophysical Research Letters*, **38 (19)**, n/a–n/a, https://doi.org/10.1029/2011gl048970, URL https://doi.org/10.1029/2011gl048970.

Stewart, E. J., S. Howell, D. Draper, J. Yackel, and A. Tivy, 2009: Sea ice in canada's arctic: Implications for cruise tourism. *ARCTIC*, **60 (4)**, https://doi.org/10.14430/arctic194, URL https://doi.org/10.14430/arctic194.

Stroeve, J., L. C. Hamilton, C. M. Bitz, and E. Blanchard-Wrigglesworth, 2014: Predicting september sea ice: Ensemble skill of the SEARCH sea ice outlook 2008-2013. *Geophysical Research Letters*, **41 (7)**, 2411–2418, https://doi.org/10.1002/2014gl059388, URL https://doi.org/10.1002/2014gl059388.

Swart, N. C., and Coauthors, 2019: The canadian earth system model version 5 (CanESM5.0.3). *Geoscientific Model Development*, **12 (11)**, 4823–4873, https://doi.org/10.5194/gmd-12-4823-2019.

Thorndike, A. S., D. A. Rothrock, G. A. Maykut, and R. Colony, 1975: The thickness distribution of sea ice. *Journal of Geophysical Research*, **80 (33)**, 4501–4513, https://doi.org/10.1029/jc080i033p04501, URL https://doi.org/10.1029/jc080i033p04501.

Tietsche, S., D. Notz, J. H. Jungclaus, and J. Marotzke, 2013: Predictability of large interannual arctic sea-ice anomalies. *Climate Dynamics*, **41 (9-10)**, 2511–2526, https://doi.org/10.1007/s00382-013-1698-8, URL https://doi.org/10.1007/s00382-013-1698-8.

Tremblay, L. B., G. A. Schmidt, S. Pfirman, R. Newton, and P. DeRepentigny, 2015: Is ice-rafted sediment in a north pole marine record evidence for perennial sea-ice cover? *Philosophical Transactions of the Royal Society A: Mathematical, Physical and Engineering Sciences*, **373 (2052)**, 20140 168, https://doi.org/10.1098/rsta.2014.0168, URL https://doi.org/10.1098/rsta.2014.0168.

Vincent, W. F., and Coauthors, 2011: Ecological implications of changes in the arctic cryosphere. *AMBIO*, **40 (S1)**, 87–99, https://doi.org/10.1007/s13280-011-0218-5, URL https://doi.org/10.1007/s13280-011-0218-5.

Voldoire, A., and Coauthors, 2019: Evaluation of CMIP6 DECK experiments with CNRM-CM6-1. *Journal of Advances in Modeling Earth Systems*, **11 (7)**, 2177–2213, https://doi.org/10.1029/2019ms001683.

Wang, J., L. A. Mysak, and R. G. Ingram, 1994: Interannual variability of sea-ice cover in hudson bay, baffin bay and the labrador sea. *Atmosphere-Ocean*, **32 (2)**, 421–447, https://doi.org/10.1080/07055900.1994.9649505, URL https://doi.org/10.1080/07055900.1994.9649505.

Williams, J., B. Tremblay, R. Newton, and R. Allard, 2016: Dynamic preconditioning of the minimum september sea-ice extent. *J. Climate*, **29**, 5879–5891, https://doi.org/10.1175/JCLI-D-15-0515.1.

Zhan, Y., and R. Davies, 2017: September arctic sea ice extent indicated by june reflected solar radiation. *Journal of Geophysical Research: Atmospheres*, **122 (4)**, 2194–2202, https://doi.org/10.1002/2016jd025819, URL https://doi.org/10.1002/2016jd025819.

Zhang, J., R. Lindsay, A. Schweiger, and I. Rigor, 2012: Recent changes in the dynamic properties of declining arctic sea ice: A model study. *Geophysical Research Letters*, **39 (20)**, https://doi.org/10.1029/2012gl053545, URL https://doi.org/10.1029/2012gl053545.

Zhang, J., and D. A. Rothrock, 2003: Modeling global sea ice with a thickness and enthalpy distribution model in generalized curvilinear coordinates. *Monthly Weather Review*, **131 (5)**, 845–861, https://doi.org/10.1175/1520-0493(2003)131<0845:mgsiwa>2.0.co;2, URL https://doi.org/10.1175/1520-0493(2003)131<0845:mgsiwa>2.0.co;2.